Article

Investigation of Microstructure, Nanohardness and Corrosion Resistance for Oxi-Nitrocarburized Low Carbon Steel

Young-Wook Cho [1], Young-Joon Kang [1], Ju-Hwan Baek [1], Jeong-Ho Woo [2] and Young-Rae Cho [1,*]

[1] School of Materials Science and Engineering, Pusan National University, Busan 46241, Korea; choyw@pusan.ac.kr (Y.-W.C.); dudhjpo@pusan.ac.kr (Y.-J.K.); bbn1004@pusan.ac.kr (J.-H.B.)

[2] Korea Clad Tech Co. Ltd., Guji-myeon, Dalseong-gun, Daegu 48013, Korea; jh_woo@koreaclad.com

[*] Correspondence: yescho@pusan.ac.kr; Tel.: +82-51-510-2389

check for updates

Abstract: A role of oxi-nitrocarburizing technique for low-carbon steel was intensively evaluated as a means of reducing the problem of corrosion in gas nitrocarburizing, which is a vital disadvantage of gas nitrocarburizing. Oxi-nitrocarburizing was carried out by a two-step process: Gas nitrocarburizing at 560 °C and oxidation. In order to characterize two different methods of oxi-nitrocarburizing, oxidation was performed under two different conditions: Air and steam as oxygen sources. To analyze the microstructural, physical, and chemical properties of the thin oxide layer and nitride layer, which are the surface hardened layers formed on low-carbon steel by oxi-nitrocarburizing, several methods, such as electron probe microanalysis (EPMA), electron backscattered diffraction (EBSD), scanning electron microscopy (SEM), nanoindentation tests, and potentiodynamic polarization tests were applied. The results indicated that the EPMA and EBSD methods are powerful techniques for the analysis of microstructure, such as phase analysis and metallic element distribution in the oxide layer of magnetite and compound layer of ε-phase and γ'-phase, for oxi-nitrocarburized low-carbon steel. Additionally, the nanohardness using the nanoindentation test and corrosion resistance using the potentiodynamic polarization test for the oxi-nitrocarburized specimens are useful methods to understand the mechanical and corrosion properties of the surface hardened layer.

Keywords: oxi-nitrocarburizing; low-carbon steel; microstructure; nanoindentation; corrosion resistance

1. Introduction

Along with the advances in industry, the surface heat treatment of steel used for component materials is an essential technology for improving their durability. Over the last few decades, the importance of surface heat treatment has increased owing to the easily improved physical and chemical properties at a low cost. In particular, nitriding and carburizing, which are typical chemical heat treatment techniques for surface heat treatment, have been applied widely to component parts for transportation machines, which require high wear resistance [1–3].

As steel nitridation is performed at relatively low temperatures, from 550 to 590 °C, which is in the ferrite region, quenching is not required and the amount of deformation is small when compared to carburizing, which requires a high temperature process of 900 °C or more. When steel is nitrided, a compound layer and diffusion layer are formed on the steel's surface. Several nitriding methods are used, such as gas nitriding, salt bath nitriding, and plasma nitriding. Of these methods, gas nitridation is used most widely because of its various merits [3]. A deep surface hardened layer in the range of several hundred micrometers can be obtained by gas nitriding. For gas nitriding, however, the

process time should be as long as several tens of hours. Additionally, only high-grade steel is suitable. Furthermore, the nitride layer formed during gas nitridation must be removed before practical use because of its high brittleness. To overcome the problems with gas nitriding, gas nitrocarburizing technology has been developed [4,5].

Gas nitrocarburizing is a process in which nitrogen and carbon are supplied and diffused into a steel surface at the same time. Gas nitrocarburizing has some advantages over gas nitriding: A short treatment time of several hours and wide applicability of steel, including low carbon steels. Therefore, gas nitrocarburizing has been widely applied to the development of component materials requiring high wear resistance. Despite this, the surface of steel formed by gas nitrocarburizing is mainly composed of two nitride layers: Epsilon(ε)-phase and gamma prime(γ')-phase, which have high wear resistance but insufficient corrosion resistance. The carbon concentration of the surface determines the dominant phase. Low-carbon steel produces a dominant gamma prime-phase, however high-carbon steel produces a dominant epsilon phase [5,6].

An oxi-nitrocarburizing technique was developed to reduce the corrosion rates, which is a disadvantage of gas nitrocarburizing. Oxi-nitrocarburizing consists of two steps: Gas nitrocarburizing of the surface and oxidation of the specimen surface [5–8]. When oxidation is additionally processed after gas nitrocarburizing, the corrosion resistance of a specimen can be considerably improved because an oxide layer is formed on the surface of the porous ε-phase in the nitride layer [7]. On the other hand, systematic research on the microstructure, mechanical, and chemical properties of the surface hardened layer is insufficient because the thickness of the oxide layer can be as thin as a few μm or less. Furthermore, research on nanoindentation for the surface hardened layer has rarely been done.

The objective of this study is to investigate the microstructure, nanohardness, and corrosion resistance of oxi-nitrocarburized low-carbon steels. We carefully analyzed the properties of the thin oxide layer and nitride layer, which are the surface hardened layers formed on low-carbon steel by oxi-nitrocarburizing. The microstructure, nanohardness, and corrosion resistance were evaluated using EPMA and EBSD, nanoindentation tests, and potentiodynamic polarization tests, respectively.

2. Materials and Methods

A steel plate cold commercial (SPCC), which is a type of extremely low-carbon steel for cold rolling, produced by POSCO, with a thickness of 0.8 mm, was used as the raw material. Table 1 lists the main composition of the SPCC used in this study. A small amount of manganese (Mn) and copper (Cu) existed as an alloy element in the iron (Fe) matrix.

Table 1. Chemical composition of SPCC steel (wt.%).

Fe	C	Mn	P	S	Cu
Bal.	0.0018	0.206	0.092	0.004	0.051

Figure 1 shows a schematic diagram of the oxi-nitrocarburizing process. Before the oxi-nitrocarburizing process, various contaminants on the surface of the SPCC were removed by shot peening. Table 2 lists the holding temperature and ratio of gases in the gas nitrocarburizing and oxidation processes. In Table 2, untreated-specimen means a raw specimen, namely before gas nitrocarburizing, and air-specimen and steam-specimen mean oxi-nitrocarburized specimens produced under different conditions in the oxidation step.
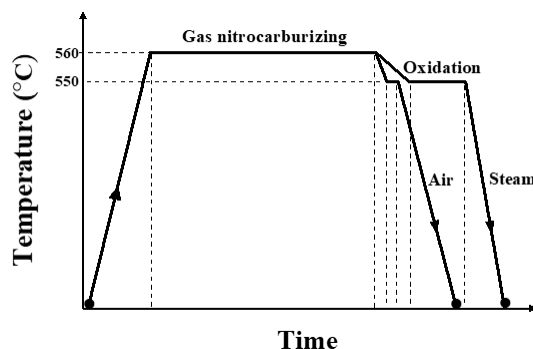
Figure 1. Schematic diagram of the surface heat treatment process in this study.

Table 2. Notation and conditions of oxi-nitrocarburizing for each specimen.

Notation	Gas Nitrocarburizing			Oxidation		
	Temp. (°C)	Input Gas Ratio (NH_3:N_2:CO_2)	Time (min)	Temp. (°C)	Input Gas	Time (min)
Untreated-specimen	-	-	-	-	-	-
Air-specimen				550	Air	5
Steam-specimen	560	5:4:1	100	550	Steam (H_2O)	30

As shown in Figure 1 and Table 2, oxi-nitrocarburizing was performed in two steps: Gas nitrocarburizing was performed at 560 °C as the first step, and oxidation was performed at 550 °C as the second step. Gas nitrocarburizing was carried out for 100 min in an ammonia (NH_3), nitrogen (N_2), and carbon dioxide (CO_2) atmosphere, and the purity of the gases was more than 99%. After gas nitrocarburizing, oxidation was performed in air atmosphere for 5 min for the air-specimen. In contrast, for the steam-specimen, oxidation was performed in a high temperature steam (H_2O) atmosphere for 30 min. About 50 min was needed to reach the gas nitrocarburizing temperature of 560 °C, which is the temperature of the first step. After oxidation in the second step, nitrogen was injected into the chamber and cooled to approximately 100 °C to complete the oxi-nitrocarburizing process.

To examine the cross-sectional microstructure of the surface hardened layer formed by oxi-nitrocarburizing, a cross-section of the specimen was polished, etched with a 4%-Nital solution and analyzed by scanning electron microscopy (SEM). Electron probe microanalysis (EPMA) and electron backscatter diffraction (EBSD) analysis were performed to investigate the phase analysis and distribution of nitride and oxide layers in the surface hardened layer. For the EBSD analysis, an AMETEK (Model: Hikari XP EBSD Camera, AMETEK Co., Ltd., Tokyo, Japan) was used and a step size for phase analysis was fixed to 60 nm.

To examine the effects of oxi-nitrocarburizing on the surface properties of the SPCC specimen, the nanohardness and corrosion resistance were also studied. The nanohardness of the surface hardened layer was measured using a nanoindentation method after mirror-polishing the cross section of the specimen [9,10]. The nanoindentation measurements were performed using a Vickers indenter (Model: Fischerscope HM2000, Fischer Technology Inc., Windsor, CO, USA), and the nanohardness was obtained by averaging five measurements using a small load of 10 mN. During the nanoindentation measurement, the time for loading and unloading were 10 s, respectively.

The corrosion resistance was examined according to the oxidation conditions through a potentiodynamic polarization test. An aqueous 3.5% NaCl solution was used for the electrolyte and a saturated calomel electrode (SCE) was used as the standard electrode for measuring the potential. Platinum (Pt) was used as a counter electrode and the exposed area of the specimen was fixed to 1.0 cm^2.

3. Results and Discussion

3.1. Microstructure and Phase Analysis

Figure 2a,b shows cross-sectional SEM images of the air-specimen and steam-specimen. As shown in Table 1, the raw material used in this study is extremely low-carbon steel with a C content of 0.0018 wt.%. Therefore, the surface hardened layer formed by gas nitrocarburizing of the specimens used in this study is similar to that of other studies, in that a surface hardened layer is composed of a porous ε-phase, massive ε-phase, and γ'-phase processed by gas nitrocarburizing low-carbon steels [3,11]. Based on the SEM image shown in Figure 2, the EPMA and EBSD study were performed from a microstructural view point including phase and metallic element distribution.
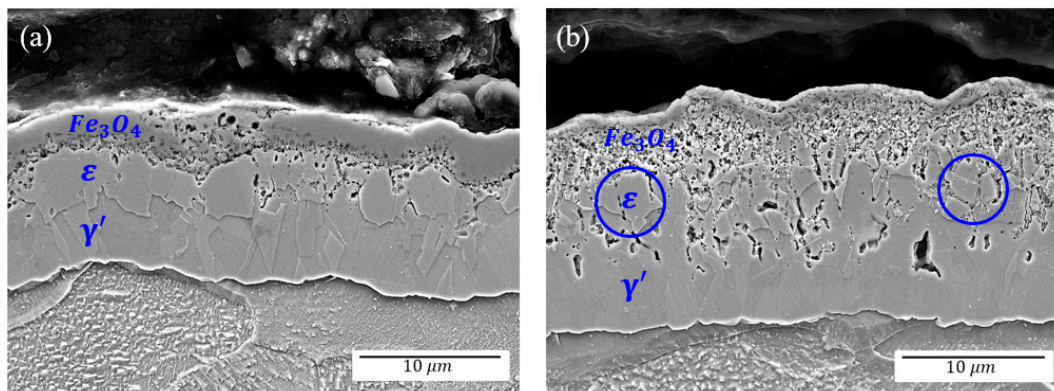

Figure 2. SEM images of surface hardened layer: (**a**) air-specimen and (**b**) steam-specimen.

Figure 3 presents the element mapping results for oxygen (O) and nitrogen (N) on the surface hardened layer of the oxi-nitrocarburized specimens using air and steam by EPMA. Figure 3a–c shows the air-specimen. Figure 3d–f is shows the steam-specimen.
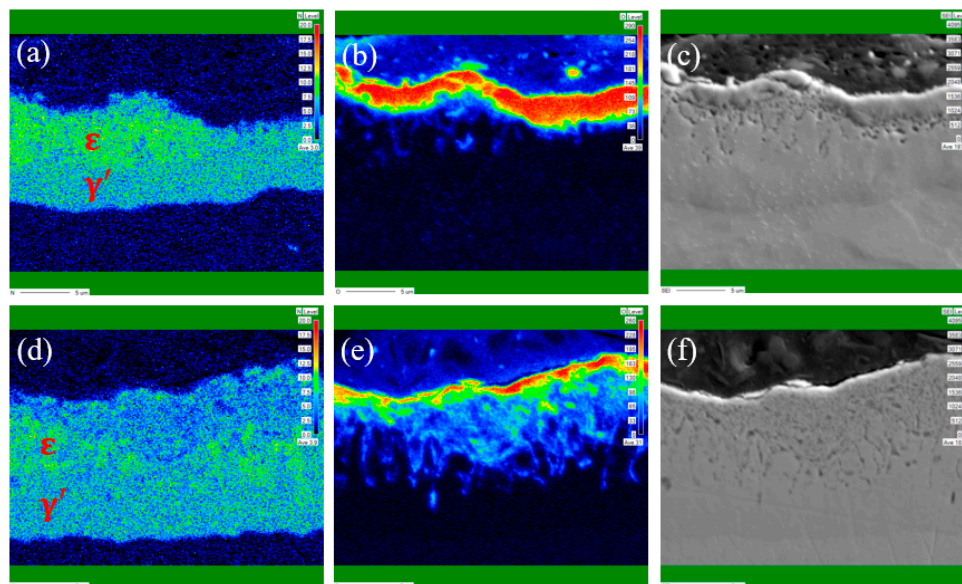

Figure 3. EPMA results for surface hardened layer: (**a**) element map of N, (**b**) element map of O and (**c**) SEM image of the air-specimen, (**d**) element map of N, (**e**) element map of O and (**f**) SEM image of the steam-specimen.

As shown in the nitrogen elemental maps in Figure 3a,d, the compound layer exists as two phases (ε, γ') with different nitrogen contents. The region with relatively high nitrogen content

is the ε-phase(Fe$_{2-3}$N) and the region with low nitrogen content is the γ'-phase(Fe$_4$N) [8,11]. The air-specimen has a compound layer with a mean thickness of 8 µm, which is composed of a massive, continuous ε-phase and γ'-phase. On the other hand, the steam-specimen revealed a compound layer with a thickness of approximately 11 µm, in which relatively small and isolated grains of ε-phase existed in the γ'-phase. Generally, the oxidation process provided an annealing effect on the compound layer, which caused the ε-phase to decompose to the γ'-phase and the nitrogen to redistribute [1,12,13]. Through the redistribution of nitrogen during the oxidation step, the γ'-phase grew and the thickness of the compound layer of the steam-specimen increased. In this manner, the volume fraction of the ε-phase in the compound layer decreased for the steam-specimen [12,13].

Figure 3b,e shows elemental maps of oxygen for each specimen. In the air-specimen, most of the oxygen was concentrated on the surface layer in the range of 2 µm. On the other hand, the distribution of oxygen in the steam-specimen was deeply spread from the surface with a range of 3–5 µm. From the SEM images in Figure 3c,f, a porous microstructure is clearly observed in the surface hardened layer.

During the oxidation process, iron-based nitride like the ε-phase will decompose into Fe and nitrogen gas, and the oxide layer could be grown continuously by supplying Fe from the ε-phase [12]. As the Fe cations migrate from the ε-phase to the oxide layer, a vacancy is generated in the ε-phase adjacent to the oxide layer [13]. In the case of the steam-specimen, the oxygen ratio in the oxidation process was high, which promoted oxide formation. Additionally, the oxidation time for the steam-specimen is also longer than that for the air-specimen. These two factors contributed that the porosity in the ε-phase adjacent to the oxide increased further, and a larger amount of oxygen penetration occurred in the steam-specimen due to the increase in porosity [1,13]. Therefore, the oxide layer could be formed deeper into the steam-specimen.

Figure 4a,b highlights the EBSD results for phase analysis of the microstructure for the surface hardened layer in the air and steam-specimens. In Figure 4a,b, the red, green, and yellow colors represent magnetite(Fe$_3$O$_4$) with a face-centered cubic (FCC) structure, ε-phase(Fe$_{2-3}$N) with a hexagonal close-packed (HCP) structure, and γ'-phase(Fe$_4$N) with FCC structure, respectively [14,15]. For the air-specimen, an oxide layer with a thickness of 2 µm covered the porous ε-phase, similar to the results shown in Figure 3. Additionally, the continuous and massive ε-phase and γ'-phase constituted the compound layer with a thickness of 8 µm. On the other hand, in the case of the steam-specimen, the oxide layer extended to a depth of 5 µm from the surface. Additionally, the thickness of the compound layer increased to 11 µm, in which a small and isolated ε-phase was surrounded by the γ'-phase. From this result, we can conclude that the EBSD is a powerful technique for the analysis of phase distribution in surface hardened layer.
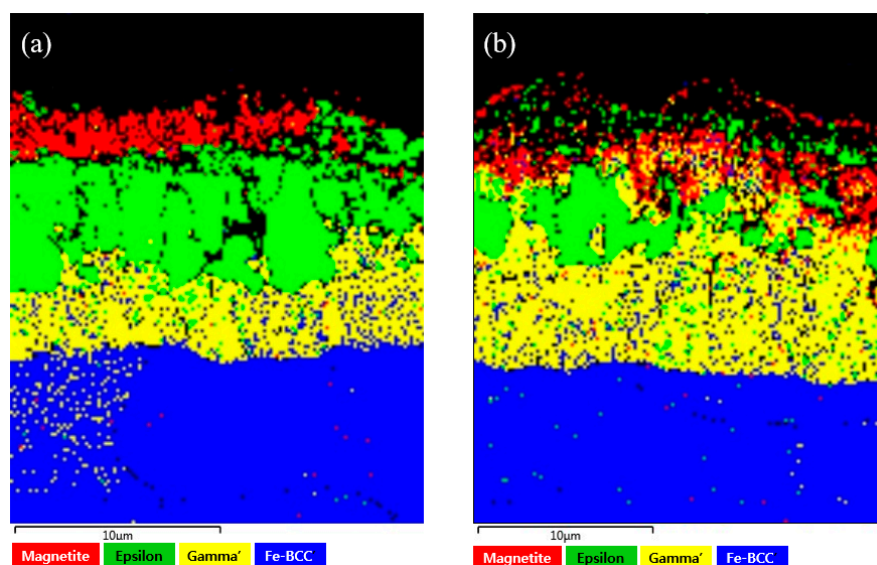

Figure 4. EBSD results for surface hardened layer: (**a**) air-specimen and (**b**) steam-specimen.

During oxidation after gas nitrocarburizing, the growth rate of the oxide layer was governed by the oxygen transfer rate from the gas phase to the interior of the Fe matrix. That is, the formation and growth of the oxide layer became easier by increasing the amount of oxygen in the supplied gas. In the case of the steam-specimen, the ratio of oxygen in the injected gas was 33.3%, which is higher than the oxygen ratio of 21% in air. In the oxidation process for the steam-specimen, a longer oxidation time and a higher oxygen content were processed. Therefore, the steam-specimen could have a characteristic of a thicker oxide layer and a porous microstructure in the ε-phase. Since the structure of the oxide layer is affected by the porosity of the ε-phase, a porous oxide layer would form on the highly porous ε-phase in the case of the steam-specimen, unlike the dense oxide layer of the air-specimen.

Table 3 lists the major characteristics of the surface hardened layers of each specimen obtained from Figures 2–4. The thickness of the oxide layer for the steam-specimen increased from 2 μm to 5 μm, but the microstructure of the oxide layer became porous. In comparison to the air-specimen, the steam-specimen showed a thin ε-phase in the compound layer and a thick compound layer of 11 μm. This was attributed to the more phase decomposition of the ε-phase in comparison to the γ'-phase and the enhanced growth of the γ'-phase during the oxidation step of the steam-specimen.

Table 3. Characteristics of the surface hardened layer of each specimen.

Classification	Air-Specimen	Steam-Specimen
Thickness of Hardened Layer	Thin [8–12 μm]	Thick [14–16 μm]
Thickness of Oxide Layer	Thin [1.5–2.5 μm]	Thick [4–6 μm]
Microstructure of Oxide Layer	Dense	Porous
Thickness of Compound Layer	Thin [6.5–9.5 μm]	Thick [10–12 μm]
Microstructure of ε-Phase	Massive, continuous	Small and isolated in the γ'-phase

Though a direct comparison of the specimens' physical propertiesis difficult because of the different oxidation times of 5 and 30 min, the distribution of phases and metallic elements in view point of microstructure for the surface hardened layers is possible. From the results shown in Table 3, we can highlight that EPMA and EBSD are useful techniques for analysis of microstructure including the oxide layer of magnetite and compound layer of ε-phase and γ'-phase for oxi-nitrocarburized low-carbon steel.

3.2. Nanohardness of the Surface Hardened Layer

Figures 5 and 6 show SEM images and representative impressions of the indenter after nanoindentation measurements for the surface hardened layer of the air and steam-specimens when the load is as small as 10 mN. In Figures 5 and 6, (a) shows SEM images of each sample, and (b), (c) and (d) show the magnetite, ε-phase, and γ'-phase, respectively. Figure 7 shows the nanohardness for each phase constituting the surface hardened layer of two oxi-nitrocarburized specimens and an untreated specimen.

From Figures 5 and 6, we can find that the impressions of the indenter can be located in the phase where we intended. The impression sizes seem too big to yield valid results for the nanohardness of the single oxide layer or nitride layer. For the measurement of the magnetite phase, the nanohardness may be influenced by the adjacent free surface. Despite the nanohardness measured by this method being not precise enough, it is worth measuring the nanohardness to understand the cross-sectional microstructure for the surface hardened layer.
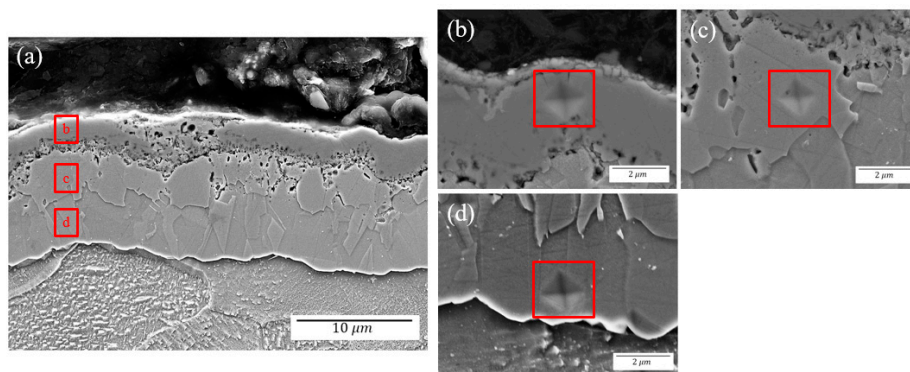
Figure 5. SEM image and impression of indenter on each phase after nanohardness test for air-specimen: (**a**) SEM image; (**b**) magnetite; (**c**) epsilon; (**d**) gamma prime.
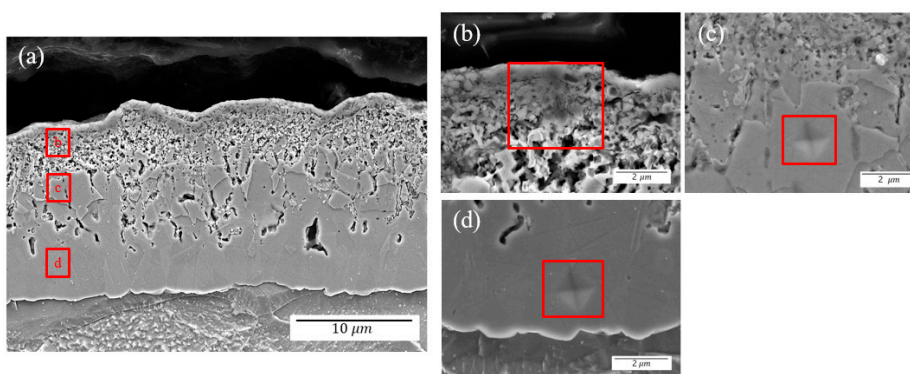

Figure 6. SEM image and impression of indenter on each phase after nanohardness test for steam-specimen: (**a**) SEM image; (**b**) magnetite; (**c**) epsilon; (**d**) gamma prime.
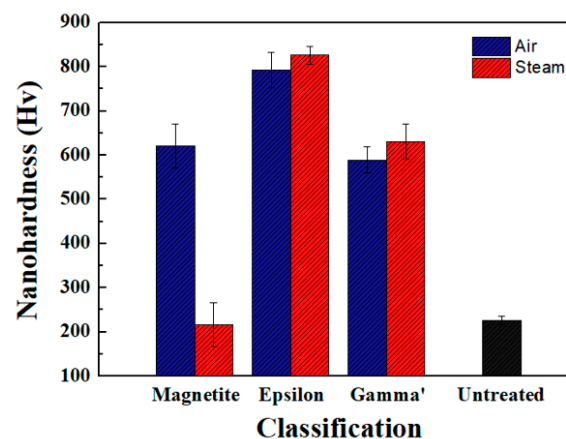

Figure 7. Nanohardness of each phase for three different specimens measured by nanoindentation with an applied load of 10 mN.

For the air-specimen, the nanohardness of the oxide layer was 621 Hv, and those of the ε and γ'-phases were 793 Hv and 589 Hv, respectively. For the steam-specimen, the nanohardness of the ε-phase and γ'-phase was 826 Hv and 631 Hv, respectively, which are 30–40 Hv higher than that of the nitride layer of the air-specimen. On the other hand, the nanohardness of the oxide layer was 216 Hv, which is much lower than that of the oxide layer of the air-specimen. In general, the hardness of the surface hardened layer decreases with the formation of the oxide layer due to the low hardness of the oxide in comparison to the nitride [4,13]. Furthermore, the nanohardness of the oxide layer in the steam-specimen showed a greatly reduced value of 216 Hv, and the nanohardness showed large

deviations. As shown in Table 3, the low and large deviation in nanohardness for the steam-specimen is due to the porous microstructure of the oxide layer [16,17].

A qualitative comparison of the nanohardness of the air-specimen and steam-specimen showed that the nanohardness of the ε-phase and γ'-phase constituting the compound layer had a similar tendency, but the nanohardness of the steam-specimen showed higher than that of the air-specimen. This is because the nitrogen concentration in the ε-phase and γ'-phase increased due to the annealing effect imparted by the oxidation process [12,13]. That is, the nitrogen concentration in the ε-phase and γ'-phase increased as the oxidation process proceeded, which made the nanohardness of the compound layer increase.

3.3. Corrosion Resistance

Figure 8 shows the representative results of the potentiodynamic polarization test for three different specimens. The polarization curves of the air-specimen and the steam-specimen were shifted to a higher potential and lower current density direction than those of the untreated-specimen.
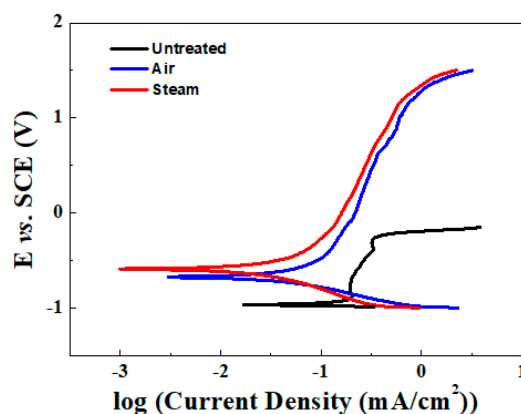

Figure 8. Potentiodynamic polarization curves of the three different specimens.

Table 4 lists the corrosion potential and corrosion current density calculated by a Tafel extrapolation from the polarization curves of Figure 8. The corrosion potential of the untreated-specimen was lowest with a value of -0.97 V, and the corrosion potential of the air-specimen and steam-specimen were -0.77 V and -0.75 V, respectively, which is a higher value than that of the untreated-specimen. On the other hand, the corrosion current densities of the air and steam-specimens were 0.087 mA/cm^2 and 0.071 mA/cm^2, respectively. These values are much lower than that of the untreated-specimen (0.184 mA/cm^2). The results in Figure 8 and Table 4 indicate that the corrosion resistance of the oxi-nitrocarburized specimen is better than that of the untreated-specimen.

Table 4. Corrosion potential and corrosion current density for each specimen.

Specimen	Corrosion Potential (V)	Current Density (mA/cm^2)
Untreated	-0.97	0.184
Air	-0.77	0.087
Steam	-0.75	0.071

As shown in Table 4, regardless of the oxidation conditions, the corrosion resistance of the oxi-nitrocarburized specimens showed superior performance when compared to the untreated-specimens. This means that oxi-nitrocarburizing is a potential method for improving the corrosion resistance due to the formation of a magnetite oxide layer, which is chemically stable and fills the porous microstructure of the nitride layer [18–20]. In particular, a comparison of Tables 3

and 4 showed that the best corrosion resistance of the steam-specimen is due to the thicker oxide layer which has a porous microstructure.

4. Conclusions

In order to investigate the microstructure, nanohardness, and corrosion resistance for oxi-nitrocarburized low-carbon steels, we carefully analyzed the properties of the surface hardened layer and the following conclusions were obtained:

- EPMA and EBSD methods are useful techniques for analysis of microstructure including the oxide layer of magnetite and compound layer of ε-phase and γ'-phase for oxi-nitrocarburized low-carbon steel.
- Though the nanohardness measured by nanoindentation method is not precise enough, it is worth measuring the nanohardness to understand the cross-sectional microstructure for the surface hardened layer.
- Regardless of the oxidation conditions, the corrosion resistance of the oxi-nitrocarburized specimens showed superior performance when compared to the untreated-specimens. This means that oxi-nitrocarburizing is a potential method for improving the corrosion resistance because of the formation of a thicker magnetite oxide layer.

Author Contributions: Y.-W.C., Y.-J.K., J.-H.B., J.-H.W., and Y.-R.C. conceived and designed the experiments; Y.-W.C. performed the experiments; Y.-W.C. and Y.-R.C. analyzed the data and wrote this paper.

Conflicts of Interest: The authors declare no conflict of interest.

References

1. Hoppe, S. Fundamentals and applications of the combination of plasma nitrocarburizing and oxidizing. *Surf. Coat. Technol.* **1998**, *98*, 1194–1204. [CrossRef]
2. Lee, I. Plasma Nitrocarburizing Technique with Quenching and Tempering for Manufacture of Vehicle Parts. *Korean J. Met. Mater.* **2015**, *53*, 398–405. [CrossRef]
3. Lee, W.B.; Yu, K.C.; Kim, Y.M.; Wi, J.L. Microstructural Evolution of Compound Layers During Gaseous Nitriding of AISI1045 Carbon Steels. *Korean J. Met. Mater.* **2016**, *54*, 457–482. [CrossRef]
4. Jeong, E.K.; Park, I.M.; Lee, I. Plasma post-oxidation of nitrocarburized SUM 24L steel. *Mater. Sci. Eng. A* **2007**, *449–451*, 868–871. [CrossRef]
5. Lee, I. Post-oxidizing treatments of the compound layer on the AISI 4135 steel produced by plasma nitrocarburizing. *Surf. Coat. Technol.* **2004**, *188–189*, 669–674. [CrossRef]
6. Kim, H.K.; Kim, Y.H. Effects of Heat Treatment on Corrosion Resistance Properties of Gas Nitrided Stainless Steels. *J. Korean Soc. Heat Treat.* **2009**, *22*, 298–306.
7. Moon, K.I.; Kim, S.K.; Kim, S.W. A Study on the Corrosion Resistance of Free Cutting Steels after Oxy-Nitriding. *J. Korean Soc. Heat Treat.* **2006**, *19*, 90–95.
8. Jacquet, P.; Coudert, J.B.; Lourdin, P. How different steel grades react to a salt bath nitrocarburizing and post-oxidation process: Influence of alloying elements. *Surf. Coat. Technol.* **2011**, *205*, 4064–4067. [CrossRef]
9. Cho, Y.R.; Fromm, E. The New Measuring Technology for Adhesion Strength of TiN or Al coatings on HSS Substrates. *Korean J. Met. Mater.* **1995**, *5*, 310–315.
10. Kim, Y.C.; Gwak, E.J.; Ahn, S.M.; Han, H.N.; Kim, J.Y. Indentation size effect in nanoporous gold. *Acta Mater.* **2017**, *138*, 52–60. [CrossRef]
11. Somers, M.A.J.; Mittemeijer, E.J. Formation and Growth of Compound Layer on Nitrocarburizing Iron: Kinetics and Microstructural Evolution. *Surf. Eng.* **1987**, *3*, 123–137. [CrossRef]
12. Jutte, R.H.; Kooi, B.J.; Somers, M.A.J.; Mittemeijer, E.J. On the oxidation of α-Fe and ε-Fe$_2$N$_{1-z}$: I. Oxidation kinetics and microstructural evolution of the oxide and nitride layers. *Oxid. Met.* **1997**, *48*, 87–109. [CrossRef]

13. Fares, M.L.; Chaoui, K.; Le coze, J. Post-oxidizing effects on surface characteristics of salt bath nitrocarburized AISI 02 tool steel type. *Surf. Interface Anal.* **2009**, *41*, 549–559. [CrossRef]

14. Leineweber, A.; Jacobs, H. Theoretical analysis of occupational ordering in hexagonal interstitial compounds: Carbides, nitrides and oxides with "ε-type" superstructures. *J. Alloys Compd.* **2000**, *308*, 178–188. [CrossRef]

15. Zlatanović, M.; Popović, N.; Bogdanov, Ž.; Zlatanvic, S. Plasma post oxidation of nitrocarburized hot work steel samples. *Surf. Coat. Technol.* **2004**, *177–178*, 277–283. [CrossRef]

16. Luo, J.; Stevens, R. Porosity-dependence of elastic moduli and hardness of 3Y-TZP ceramics. *Ceram. Int.* **1999**, *25*, 281–286. [CrossRef]

17. Tang, Q.; Gong, J. Effect of porosity on the microhardness testing of brittle ceramics: A case study on the system of NiO–ZrO$_2$. *Ceram. Int.* **2013**, *39*, 8751–8759. [CrossRef]

18. Abedi, H.R.; Salehi, M.; Yazadkhasti, M.; Hemmasian-E, A. Effect of high temperature post-oxidizing on tribological and corrosion behavior of plasma nitrided AISI 316 austenitic stainless steel. *Vacuum* **2010**, *85*, 443–447. [CrossRef]

19. Sohi, M.H.; Ebrahimi, M.; Raouf, A.H.; Mahboubi, F. Comparative study of the corrosion behaviour of plasma nitrocarburised AISI 4140 steel before and after post-oxidation. *Mater. Des.* **2010**, *31*, 4432–4437. [CrossRef]

20. Cho, Y.W.; Won, J.H.; Woo, J.H.; Yu, S.H.; Cho, Y.R. Effect of Oxi-Nitrocarburizing on the Microstructure, Nanohardness and Corrosion Properties for Low Carbon Steel. *Korean J. Met. Mater.* **2018**, *56*, 289–295. [CrossRef]